

State of the art experimental apparatus for fast entangling gates in trapped multi-ion crystals

Donovan Webb

Department of Physics, University of Oxford

E-mail: donovan.webb@physics.ox.ac.uk

Abstract.

Scalable trapped-ion quantum computation relies on the development of high-fidelity fast entangling gates in many ion crystals. Currently the speed of geometric phase gates are limited by either large scattering errors (with Raman transitions) or off-resonant carrier excitations (with quadrupole transitions). Utilizing standing waves offers a potential pathway to achieve fast entanglement in quadrupole transitions due to suppressing undesired carrier excitations. Using a legacy apparatus we present initial results of this carrier suppression in the 674-nm quadrupole transition of $^{88}\text{Sr}^+$. We demonstrate fast two-qubit entangling gates which exceed the entangling “speed limit” imposed by off resonant carrier excitations. To explore these fast gates at durations comparable to the secular trap frequency, and in multi-ion chains, a new system is been constructed. This system will use a microfabricated, segmented 3D Paul trap for greater control of long ion chains, and will feature single ion addressing for both selective and high power coherent operations. We will use $^{40}\text{Ca}^+$ which has a quadrupole transition of 729-nm. We present the current progress and roadmap of this next-generation platform and motivations behind design choices.

1. Introduction

Previously the physicist was limited to thought experiments on the Quantum nature of single particles. It was inconceivable to isolate, probe, and entangle at the single particle scale. However the advent of ion traps, specifically Paul and Penning traps, have enabled the experimental exploration and corroboration of atomic theory, producing incredibly precise measurements such as XXclocks, relativity, g factorXX [clocks, relativity, g factor].

With the high degree of experimental control of a quantum system exhibited by ion trap systems, they are a popular and increasingly mature platform for enabling Quantum Computation (QC).

The ion trap platform is a promising candidate for noisy intermediate scale QC (NISQ) due to its high single and two qubit fidelities and long coherence times. However the relatively long two qubit gate times greatly limits the number of consecutive operations possible whilst maintaining some fixed overall algorithm fidelity. Here we shall discuss a possible route to fast two qubit entangling gates, report on initial results from a proof of

principle experiment, and describe a new ion trap apparatus being constructed tailored for exploring fast gate operations.

Still Under Construction

Ion-traps trap ions through a combination of static and oscillating electric fields. Ions will sit at local minima of this potential and experience harmonic motion. When N ions are trapped simultaneously they may form linear strings or crystals due to the combination of trapping potential and mutual repulsion between like charged ions. A linear crystal of N ions will exhibit $3N$ normal modes of motion. These single ions within the crystal may be modelled as two level “spin” systems, whilst the harmonic motion is modelled as a “spring” system. Using either laser light or microwaves, we may drive internal spin transitions or couple together the harmonic motion with the internal spin of the ions. This spin-motion coupling may be utilized for performing entangling operations between non-neighbouring ions as their motion is shared. This interaction of a monochromatic laser interacting with an ion crystal in the Lamb-Dicke approximation is described by the Hamiltonian

$$H = \frac{\hbar\Omega}{2} e^{i\phi + i\eta(\hat{a} + \hat{a}^\dagger) - i\delta t} \hat{S}_+ + h.c.,$$

where Ω is the Rabi frequency, ϕ is the initial phase of the laser, η is the Lamb-Dicke parameter, $\hat{a}^{(\dagger)}$ is the annihilation (creation) operator for the crystal harmonic motion, δ is the detuning of the laser from the ion’s carrier transition and \hat{S}_+ is the spin operator.

- Expand this Hamiltonian to see coupling to E field and gradient of E field.
 - Describe two possible break down at faster speeds:
 - Multiple motional mode participate -> Vera
 - Quadrupole MS Carrier saturation leads to speed limit. -> Cnulling. and here include the J0 J2 plot of SDF saturation
 - Possible solution for this is to use a standing wave MS interaction. When using TW always couple to both gradient and amplitude of E field. SW gives extra degree of freedom to allow only coupling to sideband.
-

2. Carrier Nulling Results

As discussed, the use of phase-stable standing waves (SW) is a clear route to fast entangling gates on quadrupole transition qubits. Here we report experimental results of both SW single qubit gates and SW Molmer Sorensen (MS) entangling gates performed on the “Blade” apparatus.

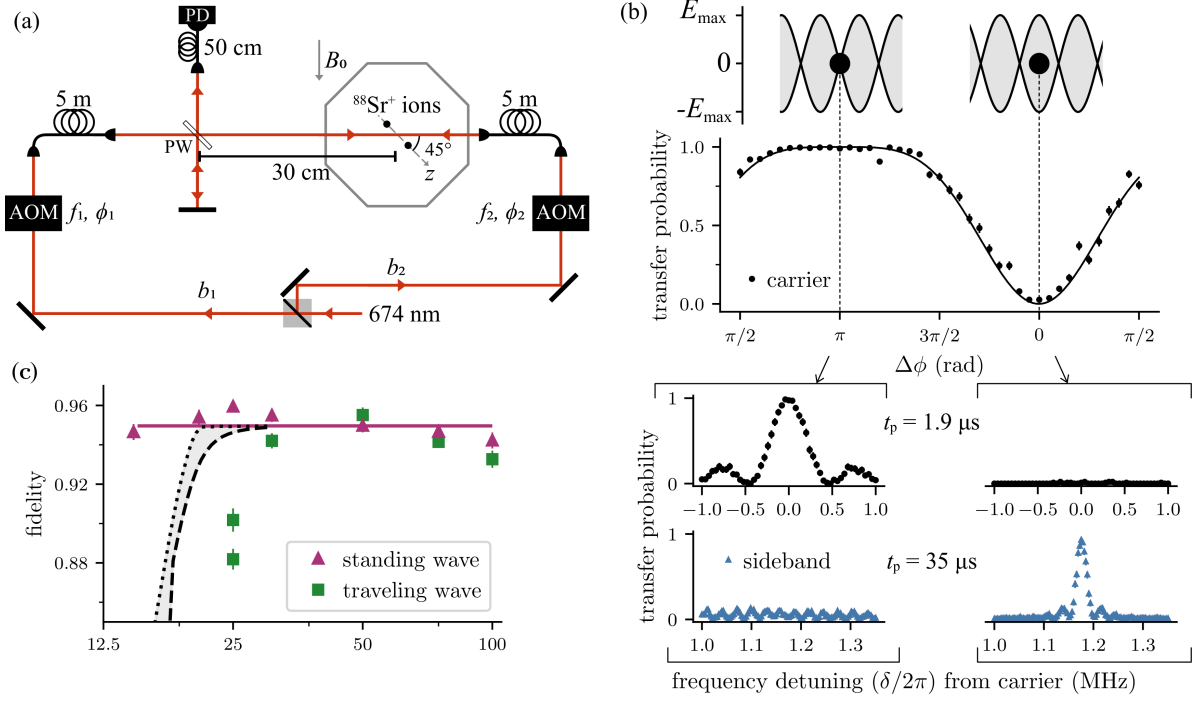


Figure 1. Carrier Null figs from [1] S. Saner and O. Băzăvan et al., ‘Breaking the entangling gate speed limit for trapped-ion qubits using a phase-stable standing wave’. arXiv, May 05, 2023.

Experimentally, the SW is formed by two superimposed counter-propagating 674-nm beams and directed onto the ions. 674-nm light couples to the quadrupole qubit transition, $5S_{1/2} \Leftrightarrow 4D_{5/2}$, in $^{88}\text{Sr}^+$. The beams propagate in free-space and are phase-stabilized to ensure the SW is stationary with respect to the ion. Figure 1 (a) displays the path of the two counter-propagating beams. AOMs are present in each branch as a switch, to apply sideband frequencies, and to control the phase of the beams. Light from each branch is picked off onto a fast photodetector to infer what phase corrections to feedback onto the AOMs. A slower secondary stabilization step is applied using the ion as a sensor. The ion is situated at what is believed to be a node of the SW and $\pi/2$ pulses on branch 1 and then immediately on branch 2 are applied. This Ramsey like sequence gives a signal sensitive to the difference in phase between the two pulses, and may be used as an error signal to also feedback onto the control AOMs.

To validate the stability and phase dependent coupling of sideband and carrier, single-qubit gates are both utilized and benchmarked. An efficient π -pulse is achieved by setting the SW to be on resonance with the qubit transition and by placing a SW node at the ion.

Figure 1 (b) shows the dependence of carrier coupling with phase of the SW seen by the ion. A monochromatic SW pulse on resonance with the qubit transition is applied.

The pulse duration corresponds to a π -pulse at maximum carrier coupling, which occurs at the nodes of the SW. For an electric quadrupole transition, the maximum carrier coupling occurs at the maximum gradient of the electric field [9]. We can maximize the carrier coupling and minimize the sideband coupling, or vice versa, by selecting $\Delta\phi = \pi$ or $\Delta\phi = 0$. The transfer probability shown in Figure 1 (b) has a quartic dependence on $\Delta\phi$ near $\Delta\phi = \pi$ and a quadratic dependence at $\Delta\phi = 0$ [26]. When probing the suppressed motional sideband, Figure. 1 (b) left, we observe only features that are due to the off-resonant (by ≈ 1.2 MHz) carrier coupling. By changing $\Delta\phi$ of the SW, we can realise any ratio between carrier and sideband coupling.

High fidelity unitary operations (gates) are essential for both near intermediate scale quantum computing [x] and for reducing overheads in required physical qubits and operations in fault-tolerant schemes [x]. To evaluate whether the phase stability of our SW is sufficient for high fidelity gates, we employ randomized benchmarking (RBM) [32]. RBM consists of applying random combinations of a pre-chosen discrete set of gates to estimate an average error per gate. We chose the one-qubit Clifford group as our set of gates to evaluate. The one-qubit Clifford group is the set of unitaries which map the Pauli matrices to one another through conjugation. There are 24 unitaries in this set. We followed the RBM protocol described in the Thesis [Amy] to evaluate our SW single qubit gates. First the qubit is prepared in some known initial state, i.e. prepared in some chosen basis. A gate sequence is then applied which consists of multiple random Clifford gates followed by a final ‘inverting’ Clifford such that the full sequence performs the Identity operation plus some error. The state is then measured in the same basis. This is repeated with the same preparation and sequence multiple times to calculate the probability that the Identity was performed - thus giving the sequence fidelity. These steps are repeated for many different random sequences with a range of sequence lengths. The sequence fidelity versus number of Clifford gates performed has now been found and a decay model is fitted to find the both the error per Clifford and the state preparation error.

Using this method we compared the single-qubit gate errors when utilizing either standing or travelling waves. We obtained an error of $1.44(3) \times 10^{-3}$ and $1.73(3) \times 10^{-3}$ per Clifford gate for the SW and TW single qubit gates, respectively. Thus, use of the SW is not detrimental to single-qubit gate fidelity. Due to spin dephasing of our quadrupole qubit originating both from natural lifetime and external noise, we took care to ensure that the duty cycle and Rabi frequency of both SW and TW RBM experiments were the same.

To explore two-qubit entangling gates we implemented an MS-type scheme with a bichromatic SW instead of the conventional bichromatic TW. The bichromatic field is created by applying two tones to the AOMs in Figure 1 (a). As with the TW MS-scheme, these tones are symmetrically detuned by $\delta \approx \pm(\omega_z + \delta_g)$ from the qubit resonance. Here ω_z is the axial mode frequency of our trapped single ion, $\omega_z = 2\pi \times 1.2$ MHz, and δ_g

is some further detuning from these sidebands. To selectively couple to the sidebands, and hence suppress the carrier term, the ion spacing is adjusted to place them both on antinodes of the bichromatic SWs.

We performed TW and SW two-qubit entangling gates on the axial in-phase mode and optimize the experimental parameters to maximize the Bell-state fidelity for a fixed gate duration. In both cases, we use a ramp duration of $10\ \mu\text{s}$ to minimize coupling to the other motional modes [33]. In Figure 1 (c), we show the two-qubit fidelities achieved with the two schemes as a function of the effective gate duration ($2\pi/\delta_g$, where $\delta_g = \delta - \omega_z$) [37]. For slower gates, the fidelity of the SW-MS is comparable with that of the TW-MS. For faster entangling gates, the fidelity of the TW-MS degrades rapidly as expected due to the carriers presence. In contrast, the fidelity for the SW-MS is consistent with ≈ 0.95 over the entire available power range, showing that we have eliminated the limit arising from the carrier coupling. The shortest SW-MS gate was $15\ \mu\text{s}$, limited by the available total power of 29 mW.

As gate duration is inversely proportional to Rabi frequency, we can further push the speed of these gates using greater intensities of light at the ions. This can be achieved by more powerful lasers or by focusing the beams down to tighter waists at the ions locations. To explore these faster gates a new apparatus has been designed and is being constructed that will feature both these improvements and will allow exploration of these gates in many ion crystals. A description and progress report of this system is described in the following section.

3. Experimental Apparatus

The technical complexity of ion trapping experiments may be reduced to solving two problems: Controlling the state of the ion (both internal and motional); and controlling the environment the ion is within. Our ion trap experiments consist of: An atomic source, a trap, a vacuum system encasing these, external magnetic field coils, and lasers for ionization, cooling, repumping, state preparation, coherent control and readout. As with all ventures in experimental physics, as technologies mature, so too do the capabilities and scope of our apparatus. Here we shall describe both the “old” apparatus, known in short as “Blade”, where proof of principle fast gate schemes have been tested, and the new proposed system known as “FastGates”, which solves critical limitations of “Blade” for further exploring fast entanglement and non-adiabatic interactions.

3.1. Ion and Trap

As mentioned, the overall system we desire is a spin coupled to a spring. Our spin in this case being a Hydrogen-like ion, and the spring being the harmonic motion of the ions within the trapping potential. The ion traps we use to create such a potential

Trap	$d / \mu\text{m}$	$\omega_{ax}, \omega_{rad} / (2\pi\text{MHz})$	\dot{n}/qs^{-1}	Trap depth / meV
Blade	500	1.9, 4	75	1000
HOA2	68	1.8, 2.5	2000	150
NPL	250	1.6*, 5.0*	<100	400*

Table 1. Comparison of different trap types at typical operating parameters. Blade is a macro blade style trap, HOA2 is a surface style trap, and NPL is a microfabricated 3D trap. d is the ion-electrode distance, ω are the motional mode frequencies for one ion, and \dot{n} is the heating rate in quanta per second. NPL starred values are from simulation. Values for Blade and HOA2 came from [Vera, Amy Thesis] and [DPN, Beth Thesis] respectively.

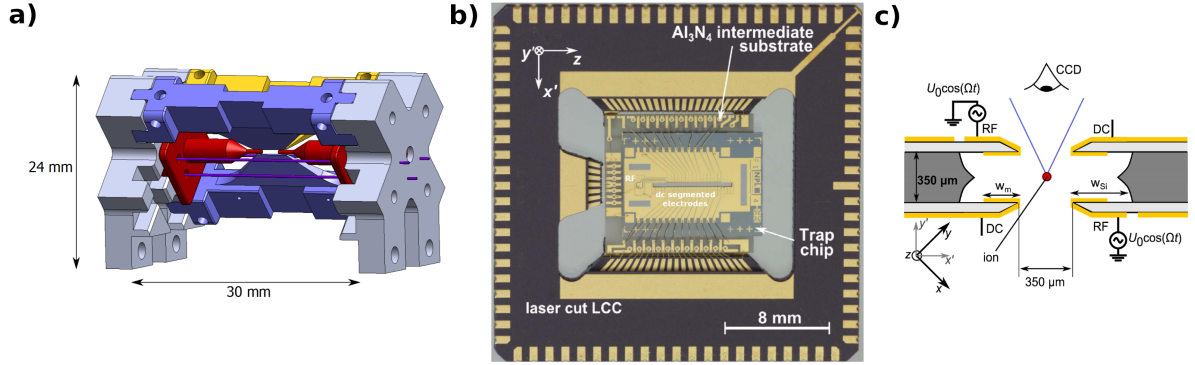


Figure 2. **a)** Blade trap used for carrier nulling results. In blue are the RF blades providing the radial pseudopotential whilst in red are the DC end caps providing the axial potential. **b)** NPL trap being used in the FastGates experiment. This is a microfabricated, segmented, multilayer trap. **c)** A cross sectional view of the NPL trap showing the RF and DC electrode positions. Figures from [S. R. Woodrow] and [K. Choonee].

are linear Paul traps, a schematic of such is shown in Figure 2 (a). As explained by Earnshaw’s theorem, ($\nabla^2 V = 0$), a stable stationary point in 3D can not be realized using only static electric potentials, V , as if the potential is confining in 2 dimensions, it will be anticonfining in the third. Therefore to achieve stable trapping an oscillating field must be utilized that create a pseudopotential. A Paul trap achieves this through an oscillating RF electric field providing radial confinement and a static field to create axial confinement. There are various popular geometries for realizing a Paul trap: Macro 3D Blade traps; surface traps; and microfabricated segmented 3D traps. A Blade trap, Figure 2 (a), as is used in the “Blade” apparatus, has axial confinement created by DC end caps and radial confinement by supplying an oscillating RF voltage to the blades. In “Blade” the ion endcap distance is 1.15 mm, and ion-blade distance is 0.5 mm. Typical operating frequency for the RF electrodes of the “Blade” trap are 28.0133 MHz leading to an axial ion frequency of 1.860 MHz and radial frequencies of 4.077 MHz and 4.341 MHz.

Recently the surface style linear Paul trap has gained popularity due to the maturity

of chip fabrication technologies and the potential route to scalability this offers. In the surface trap, the 3D blade and endcap geometry of the “macro” trap is effectively projected onto a 2D surface. The stable point of such a trap is typically on the order of 50 μm from the chip surface. The ease of fabrication of surface traps has allowed the creation of complicated multizone devices with many DC electrodes. These multizone traps enable the shuttling of ions, a requirement for Quantum CCD type architectures [ref]. However this surface style geometry greatly reduces the depth of the trapping potential and often leads to much greater heating rates. Typical values for the HOA2 trap [ref] are summarised in table 3.1. Heating of ions in a Paul trap is not well understood [ref], however empirically the ion-surface distance has a strong effect and should be maximised if possible whilst retaining an appropriate trap depth.

A microfabricated 3D trap [See et al and Wilpers 2012], as will be used in the “FastGates” apparatus, brings together the advantages of chip fabrication as well as the low heating rates and high trapping fields of a 3D style trap with greater ion-surface distances. This is achieved by a multilayer chip as shown in Figure 2 (b, c). The radial trapping is provided by RF rails on opposite diagonals of the slit whilst axial trapping may be realized by DC electrodes. The ion-surface distance is now of the order 250 μm and the heating rates have been shown to be < 100 q/s. The microfabrication techniques also allow a segmented design suitable for multizone operations and ion shuttling.

We aim for an axial ion separation of around 5 μm which, for $^{+}\text{Ca}_{40}$ ions means a trapping potential of $w_z \approx 2\pi * 1.6$ MHz. This ion separation was chosen to reduce the cross talk between ions when singly addressed (see section X). We plan for around 5 MHz for our radial frequencies as we will use one such mode for implementing two-qubit entangling gates. This higher frequency is for a few reasons. Firstly, the Doppler cooling limit ($\bar{n} = \Gamma/w$, where Γ is the transition linewidth and w is the frequency of the mode being cooled) goes with the reciprocal of the mode frequency and so higher mode frequencies leads to a lower temperature after initial cooling. Secondly, a higher center-of-mass radial mode leads to better separation and therefore participation of radial modes in a multi-ion crystal which, if we implement the amplitude pulse shaped fast gate scheme described above, can lead to pulse solutions with fewer segments for a given gate time.

Using the pseudopotential approximation for trapping, we can find a trapping frequency in one radial direction ω_p

$$\omega_p = \frac{e\alpha V_{RF}}{\sqrt{2}\Omega_{RF}M\rho^2},$$

where α is a factor of order unity given by the geometry of the trap, V_{RF} and Ω_{RF} are the voltage and frequency of the RF provided to the blades, M is the mass of the ion, and ρ is the ion-RF electrode separation. Applying some DC voltage on the axial electrodes leads to axial confinement with frequency ω_{ax} , but must defocus the radial confinements as the total curvature of the pseudopotential must remain constant,

$$\omega_{rad} = \sqrt{\omega_p^2 - \omega_{ax}^2/2}.$$

Different to the macro Blade style trap, the NPL trap focuses one of the radial modes and defocuses the other when the DC electrodes are increased due to the “cross” arrangement of DC and RF electrodes, Figure 2 (c),

$$\omega_{rad\pm} = \sqrt{\omega_p^2 - (1 \mp \beta)\omega_{ax}^2}/2,$$

where β is some factor due to the geometry of this cross arrangement. From simulation $\beta > 1$ for $\Omega_{RF} = 23$ MHz and $V_{RF} = 200$ V and so one radial mode increases with DC voltage applied and one decreases as can be seen in figureX. A possible set of

	V_{RF}	Ω_{RF}	V_{DC}	$\omega_{ax} / (2\pi\text{MHz})$	$\omega_{rad} / (2\pi\text{MHz})$	q
Experiment	200	23	-7	1.6	4.9	0.61
Loading	100	23	-2	0.8	2.0	0.25

Table 2. Simulated parameters for both “Experiment” and “Loading” settings $^{40}\text{Ca}^+$ with the NPL trap.

parameters to achieve $\omega_{ax} = 2\pi \times 1.6$ MHz and $\omega_{rad+} = 2\pi \times 4.9$ MHz can be seen on the “Experiment” trapping in table 3.1. It is known that for stable trapping $q < 0.9$, however convenient trapping of hot ions requires q to be as low as possible. To satisfy this requirement a “Loading” setting (with parameters in table 3.1) may be used with $q = 0.25$ and then the V_{RF} ramped to the “Experiment” trapping for high radial modes.

3.2. Laser systems

We have described the trapping of an ion, now we must look at our strategies for manipulating the internal states and collective motion of ion strings. Lasers are a key tool for this as highly localised, strong electric fields amplitudes and gradients can be produced.

First let us consider the $^{40}\text{Ca}^+$ energy level structure, figure X. The $^{40}\text{Ca}^+$ has no nuclear spin and is hydrogen like with only one external electron giving a (relatively) simple level structure. An external magnetic field of 5 G is applied to Zeeman split the levels. The relevant laser transitions for our planned ion trap experiment have been marked and their purpose and construction shall be discussed below.

729-nm - Coherent control: As shown in FigureX we will use the levels $4S_{1/2}$ to $3D_{5/2}$ with a 729-nm quadrupole transition to define our qubit. Therefore the 729-nm laser is used to implement single and multiqubit gates. We also use this transition, after Doppler cooling, for resolved sideband cooling to step down to near the motional ground state of the ion crystal.

The natural lifetime of the metastable $3D_{5/2}$ is around 1.1 s XrefBarton, giving a favorable fundamental limit of coherence time for our chosen qubit. This natural lifetime leads to a narrow $4S_{1/2}$ to $3D_{5/2}$ transition linewidth $\Gamma < 1$ Hz, and so demands the

use of a narrow linewidth laser. Further, we require a high light intensity at the ion to drive sideband transitions due to a low Lamb-Dicke factor for 729 transition, $\eta \approx 0.05$. Pumped Ti:Saph laser systems have been shown to be both relatively high power and narrow linewidth, making them suitable for our experiment.

Some of the 729-nm light is picked off and sent to a wavemeter to monitor the frequency however the majority is coupled to two output fibres for our experiment and another within the group. We require fibre noise cancellation as we transport the 729

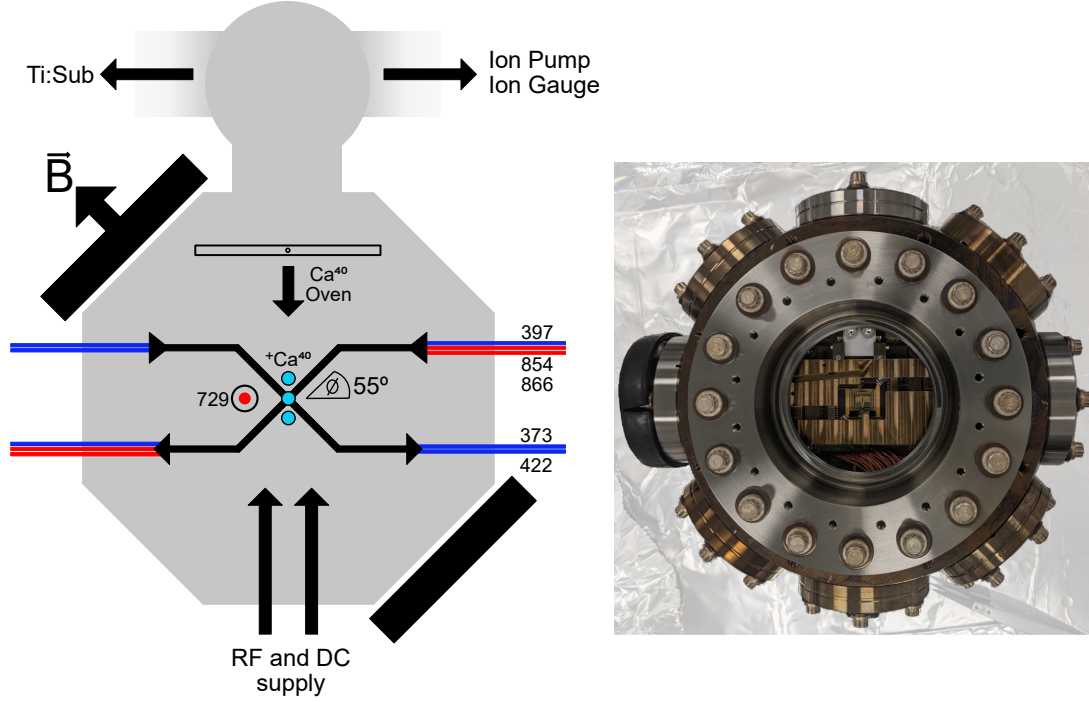


Figure 4. Vacuum can

light from a laser lab to the trapping lab by a 10 m single mode polarization maintaining fibre and must ensure no phase noise is introduced.

The remaining transitions utilize Toptica diode lasers with PDH locking on a stable cavity from Stable Laser Systems. They consist of:

- 393-nm and 432-nm - for two step photoionization with isotope selectivity
- 397-nm - for Doppler cooling and fluorescent readout.
- 854-nm and 866-nm - for repumping any lost population from the P to the D states.

3.3. Inside the vacuum

Here we shall describe the instrumentation required, and being constructed, for decoupling the ion from any unwanted external environments. Our primary tools for this are working under Ultra High Vacuum (UHV) and surrounding the vacuum system with electromagnetic shielding. Inside the vacuum system we aim for a residual pressure of less than 10^{-11} mbar. To reach this low a pressure, we must take care in material choice and thoroughly clean and bake all material within the vacuum system (a useful summary of tactics can be found in [ref]).

A schematic and photograph of the vacuum system can be seen in Figure 4. The system consists of an octagonal experimental chamber connected to an Ion pump, Ion

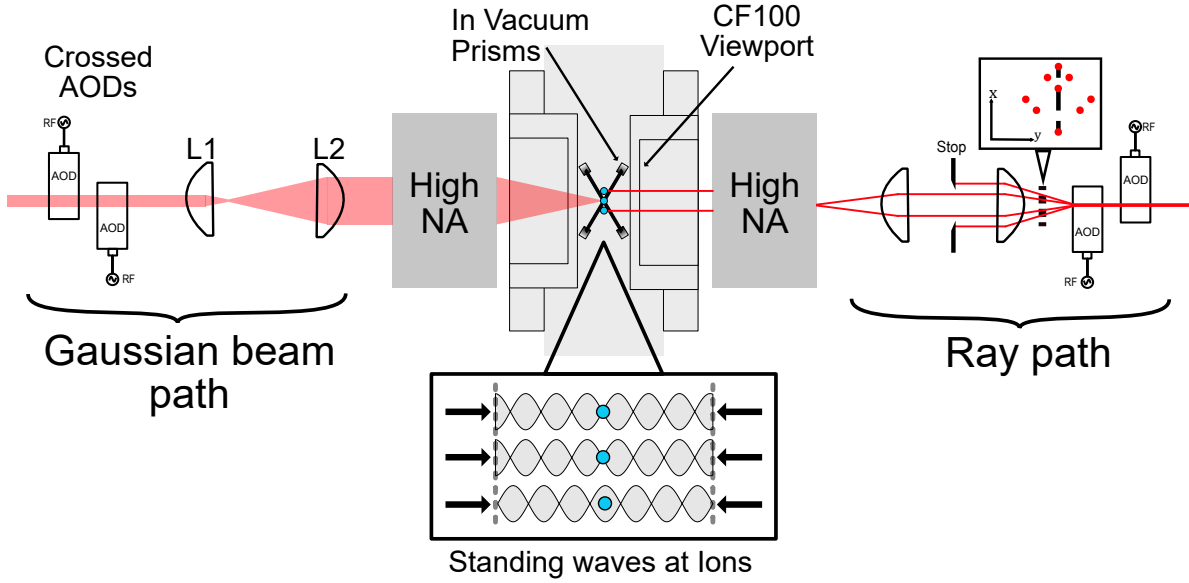


Figure 5. Single addressing system

Gauge and Ti:Sub pump. For optical access we have Dual CF100 viewports coated for 397-nm and 729-nm as well as two CF40 viewports coated for 397-nm, 422-nm, 729-nm, 854-nm and 866-nm.

As discussed above, our ion will be located within a slit of the NPL trap and so there is no visibility of the ions from the side CF40 viewports. We therefore are using in vacuum prisms to direct the light onto the ions at XX degrees.

We use an electrical feedthrough on a CF40 flange to supply our trap chip with both DC and RF voltages. As the DC cables run within close proximity to the RF supply, electrical pick up is a potential issue within our DC lines. We mitigate this through a low pass filter board within close proximity of the trap chip. We implement a “trap stack”, as can be seen in the photograph of Figure 4, within the vacuum chamber consisting of the trap chip, the outer chip carrier, an interposer, and the filter PCB.

$^{+}\text{Ca}_{40}$ was chosen for zero nuclear spin and therefore simple energy level structure. However we now cannot utilize hyperfine structure to find “clock” qubits which are insensitive to magnetic field fluctuations and must instead remove magnetic field noise from the environment. To suppress this noise we place the vacuum chamber within a box constructed from two layers of 3mm thick MuMetal [ref]. The shielding was shown to suppress the background field by a factor of 500 at its center.

3.4. Single Addressing

Still Under Construction

729 High NA (0.6) lens we can achieve waist radius of $< 1 \mu\text{m}$. With our axial trap freq of 1.6 MHz we get ion spacing of $5 \mu\text{m}$. Using AOD system we can traverse this ion chain.

- Description of lens system from AOD to ions.
- Description on the mechanism on how AOD works (this is the same as an AOM) (Probably skip this).
- Comparison between this and a fixed waveguide array. AOD have extra programmable control than waveguides which is excellent as we are in an exploratory regime where we may want to alter ion spacing/Dont want to use quartic potentials to make ions evenly spaced. There is minimal path length difference compared to waveguide which is ideal as we can stabilise at some central frequency and should be stable at all ion locations.
- We will use a crossed AOD design so that we have no overall frequency shift as we scan along the ion chain.
- Compact design to fit beam path within MuMetal box. (Probably skip this).
- Using two RF freq so that we can address two ions at the same time. Comes at cost of power due to cross terms.

4. Outlook

- Current state of building up apparatus.
 - Immediate next steps.
 - Proposed first experiments?
 - GANNT diagram?
-